Open-Source Benchmark Model for Active Flutter Suppression

Jonas Eichelsdörfer *
German Aerospace Center (DLR), 82234 Weßling, Germany

This paper presents a benchmark model for the analysis and active control of bending-torsion flutter in a flexible wing structure. The structural dynamics of a rectangular wing are modeled using a finite element (FE) beam formulation. Aerodynamic loads are computed using the planar Doublet Lattice Method (DLM), a frequency-domain linearized potential flow approach. To enable control design, the DLM results are converted to the time-domain using rational function approximation (RFA) based on Roger's method. The structural and aerodynamic models are consistently coupled, forming an aeroservoelastic plant that is controlled via distributed trailing edge flaps as well as leading edge slats. The plant is observed through distributed IMUs that measure accelerations perpendicular to the wing surface. A thorough modal analysis of the coupled system is performed, revealing the evolution of the critical aeroelastic eigenmodes with increasing freestream velocity and their velocity-dependent modal observability and controllability. The accompanying open-source MATLAB/Simulink implementation provides a practical foundation for benchmarking aeroservoelastic control strategies.

I. Introduction

Flutter is a dynamic aeroelastic instability that results from the interaction between structural vibrations and unsteady aerodynamic forces [1]. As modern aircraft design trends increasingly favor lightweight and flexible structures to enhance fuel efficiency and aerodynamic performance, the susceptibility to flutter emerges as a fundamental constraint [2]. Conventional approaches mitigate this risk through conservative structural design margins, limiting operations to airspeeds well below the open-loop flutter onset. However, active control techniques offer the potential to extend this operational boundary by artificially increasing modal damping, thereby enabling higher performance without compromising stability [3, 4].

Within the field of aeroservoelasticity, numerous studies have explored active flutter suppression using high-fidelity models of full aircraft configurations [5–9] as well as experimental wind tunnel setups [10–12]. In parallel, control theory research often focuses on academic, simplistic two-dimensional airfoil models [13–17], which, while analytically tractable, fail to capture the spatial complexity and coupling effects relevant to realistic control design [3]. Despite the abundance of studies, there remains a lack of open-access, standardized benchmark models that balance fidelity and tractability, and thus support reproducible controller development and comparative evaluation across the community.

To address this gap, this paper introduces an open-source benchmark model of a flexible rectangular wing with distributed sensors and actuators. A rectangular wing undergoing bending-torsion flutter represents the simplest configuration that still captures realistic flutter phenomenon in aircraft [18]. The structural model is constructed from a finite-element beam formulation capturing bending and torsional degrees of freedom. Aerodynamic forces are calculated using the Doublet Lattice Method (DLM) [19], a frequency-domain linear potential flow panel method that accounts for unsteady lift effects. To enable time-domain simulation and controller synthesis, the frequency-domain aerodynamic data is transformed via Rational Function Approximation (RFA), specifically using Roger's method [16, 20, 21]. The coupled structural-aerodynamic model is cast in a Linear Parameter-Varying (LPV) state-space form, where the system matrices depend explicitly on the freestream velocity. Actuation is realized via four trailing edge flaps and four leading edge slats, while sensing is accomplished through distributed inertial measurement units (IMUs).

A central contribution of this work is a detailed modal analysis of the LPV system, covering the evolution of the dominant aeroelastic modes with increasing airspeed and identifying their controllability and observability characteristics. These insights directly inform the design of sensing and actuation architectures optimized for flutter suppression and gust load alleviation. The accompanying MATLAB/Simulink implementation offers a reproducible testbed that supports both controller design and validation, thereby serving as a foundational resource for future research in aeroservoelastic control.

*Research Associate, Institute of Aeroelasticity, jonas.eichelsdoerfer@dlr.de

Paper Organization Section II presents the FE bending-torsion-beam formulation; Section III introduces the planar DLM linearized potential flow solution; In section IV the two models are consistently coupled; Section V introduces actuator and senor models; Section VI details the final LPV model used for control design. Section VII presents the results of a detailed modal analysis focused on the critical aeroelastic flutter phenomenon; A preliminary AFS control strategy is developed in section VIII; Conclusions are drawn in Section IX.

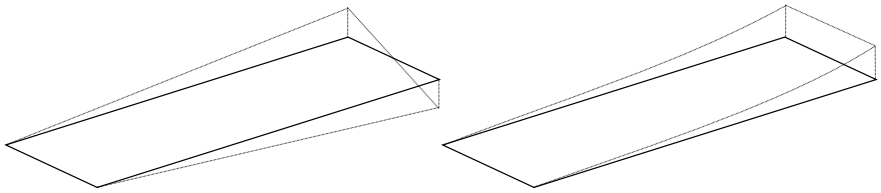

Fig. 1 Bending and Torsion
Bernoulli-Euler beam theory

II. Structural Model

The Bernoulli-Euler beam theory was chosen to model the structural bending dynamics of the generic rectangular wing. Bernoulli-Euler beam theory assumes that cross-sections remain plane and perpendicular to the neutral axis after deformation, and that shear deformations are negligible. To model torsional effects, Saint-Venant torsion theory is adopted under the assumption of linear torsional displacement. The beam undergoes:

- **bending** in the z-direction, described by the transverse displacement $u_z(y)$,
- **twisting** about the y-axis, described by the torsional angle $\psi_y(y)$.

Consider a beam element with axis along the y-direction and cross-section lying in the xz-plane. In the FEM modeling of slender structures subject to combined torsion and bending, it is critical to adopt shape functions that accurately reflect the underlying mechanics. The bending deformation is interpolated using cubic Hermite shape functions to ensure C^1 continuity of displacement, while torsion is represented using linear shape functions, suitable due to the lower-order continuity requirement. Figure 2 displays the cubic Hermitian polynomials on normalized element length. The transverse displacement as expressed in Hermitian polynomial shape functions is

$$u_z(y) = H_1(y)d_1 + H_2(y)d_2 + H_3(y)d_4 + H_4(y)d_5, \tag{1}$$

where $H_i(y)$ are the standard cubic Hermite functions defined on the interval $y \in [y_1, y_2]$. Torsional rotation is interpolated using linear shape functions

$$\psi_y(y) = N_1(y)d_3 + N_2(y)d_6. \tag{2}$$

Under Bernoulli-Euler beam theory, the rotation due to bending is $\psi_x(y) = \frac{du_z}{dy}$. The nodal degrees of freedom are

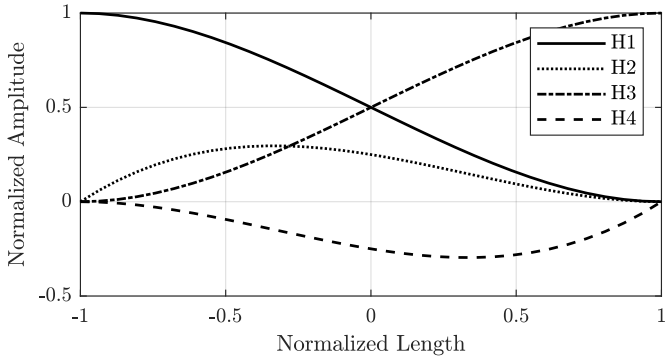

Fig. 2 Hermitian Beam Element Shape Functions.

thus: $d_1 = u_z(y_1)$ vertical displacement at node 1; $d_2 = \psi_x(y_1) = \frac{du_z}{dy}$ slope at node 1; $d_3 = \psi_y(y_1)$ torsional rotation at node 1; $d_4 = u_z(y_2)$ vertical displacement at node 2; $d_5 = \psi_x(y_2) = \frac{du_z}{dy}$ slope at node 2; and $d_6 = \psi_y(y_2)$ torsional rotation at node 2. A schematic of the nodal degrees of freedom is given in Fig. 3. The finite element discretization is

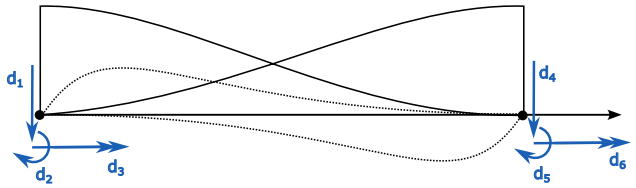

Fig. 3 Six Degrees of Freedom Beam Finite Element.

derived using the Galerkin method. The weak form of the equilibrium equations is obtained by inserting the interpolated kinematic fields $u_z(y)$ and $\psi_y(y)$ into the principle of virtual work. The Hermite shape functions $H_i(y)$ for bending and linear shape functions $N_i(y)$ for torsion are used to compute the consistent stiffness and mass matrices by integrating over the element length L. The internal strain energy V_{int} of a Bernoulli-Euler beam subject to bending and torsion over the element length L is given by:

$$V_{\text{int}} = \frac{1}{2}\int_0^L EI_{xx}^a \left(\frac{d^2u_z}{dy^2}\right)^2 dy + \frac{1}{2}\int_0^L GI_{T_y}^a \left(\frac{d\psi_y}{dy}\right)^2 dy. \tag{3}$$

This expression consists of the contributions from bending and torsional strain energy. The total kinetic energy T of the beam consists of translational kinetic energy due to the transverse motion $u_z(y)$, and rotational kinetic energy due to torsional rotation $\psi_y(y)$. The kinetic energy is given by:

$$T = \frac{1}{2}\int_0^L I_{T_y}^m \dot{\psi}_y^2\, dy + \frac{1}{2}\int_0^L \bar{\rho}\, \dot{u}_z^2\, dy - \int_0^L I_z^m\, \dot{u}_z\, \dot{\psi}_y\, dy, \tag{4}$$

Note that the leading negative sign of the coupling term is merely a consequence of the chosen sign convention for u_z and ψ_y. The following cross-sectional properties enter the formulation:

- **Bending stiffness:**

$$EI_{xx}^a = E\int_A z^2\, dA, \tag{5}$$

- **Torsional stiffness:**

$$GI_{T_y}^a = G\int_A r^2\, dA, \tag{6}$$

- **Torsional mass moment of inertia:**

$$I_{T_y}^m = \int_A r^2\rho\, dA, \tag{7}$$

- **Deviation moment:**

$$I_z^m = \int_A x\rho\, dA, \tag{8}$$

- **Mass per unit length:**

$$\bar{\rho} = \int_A \rho\, dA. \tag{9}$$

where r denotes the radial distance from the shear center (torsion axis), ρ denotes the beams mass density, E denotes Young's modulus, and G the shear modulus. Substituting the FE discretization into the equations for internal strain energy 3 and total kinetic energy 4 yields a quadratic form in the nodal displacements d_i and a quadratic form in the nodal velocities $\dot{d}_i$, respectively. The Euler-Lagrange equations for the displacement field d_i of a linear elastic solid is

$$\frac{d}{dt}\frac{\partial T}{\partial \dot{d}_i} + \frac{\partial V}{\partial d_i} = 0, \tag{10}$$

which yields the element-wise dynamic equations of motion:

$$M_{ij}^{\text{ele}}\ddot{d}_j + K_{ij}^{\text{ele}} d_j = 0. \tag{11}$$

This expression defines the entries of the consistent element mass matrix M_{ij}^{ele} corresponding to translational, torsional, and coupling contributions between displacement and rotation. Note the coupling between bending and torsion motion. This phenomenon stems from the non-coinciding elastic and mass axes. The position of the mass axis relative to the wing elastic axes is of great importance to the aeroelastic behaviour, thus must be accuratly captured by the model. In fact the addition of mass at the wing tip, i.e. moving the mass axis forward, is often a solution used by aircraft designers to prevent flutter[18]. Element stiffness and mass matrices are assembled into the global matrices by adding their contributions to the appropriate positions (DoFs) in the global stiffness and mass matrix. The resulting second order linear system is:

$$M_{gg}\ddot{q}_g + K_{gg}q_g \ = \frac{\partial V_{\text{ext}}}{\partial q_g} = F_g^{aero}. \tag{12}$$

The external forces introduced by the airflow around the lifting surface F_g^{aero} are subsequently modeled utilizing linearized potential flow theory.

III. Aerodynamic Model

The benchmark model's lifting surface is a rectangle with dimensions $c_{ref} \times s$. Importantly, its mass axis (i.e., the chordwise center of mass) does not coincide with its flexural axis. Figure 4 depicts the geometric dimensions of the wing model. For ease of implementation the models flexural axis always coincides with the y coordinate axis in this code base. To capture the effects of unsteady aerodynamic forces F_g^{aero} the Doublet Lattice Method (DLM)[16, 19, 20]

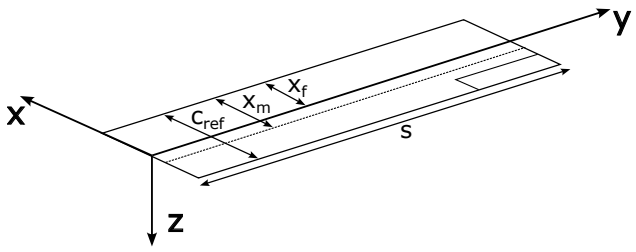

Fig. 4 Wing Model Dimensions.

is used.

A. Doublet Lattice Method

This method is rooted in classical potential flow theory and provides a linearized, frequency-domain representation of the pressure distribution on oscillating lifting surfaces. Its computational efficiency and compatibility with modal structural models make it an industry standard in preliminary aeroelastic analyses[18]. The DLM arises from linearized potential flow theory under the assumptions of inviscid, irrotational, flow. In this framework, the perturbation velocity field is derived from a scalar potential, which satisfies Laplace's equation[22]. The DLM discretizes the lifting surface into a lattice of quadrilateral aerodynamic panels. On each panel, a singularity distribution, specifically a doublet, is placed at the quarter-chord line. The influence of these doublets is evaluated at control points located at the three-quarter-chord line. The flow tangency condition is enforced at each control point in the frequency domain, assuming harmonic oscillations. Under these assumptions, the governing equations reduce to a linear system in the frequency domain. The solution yields complex-valued aerodynamic influence coefficient (AIC) matrices, denoted by $Q_{jj}(k)$, where the subscript j refers to the control points and doublet strengths / pressure difference coefficients on the surface. These matrices relate the normalized normal downwash $w_j(k)$ at the control points to the corresponding pressure difference coefficient $\Delta c_{p,j}(k)$ through the relation

$$\Delta c_{p,j}(k) = Q_{jj}(k) w_j(k), \tag{13}$$

where the reduced frequency k is defined as dimensionless frequency $k = \frac{\omega c_{\text{ref}}}{2V_\infty}$ with ω being the circular frequency, c_{ref} the reference chord, and V_∞ the freestream velocity[23]. Figure 5 displays a generic DLM Panel. C_p indicates

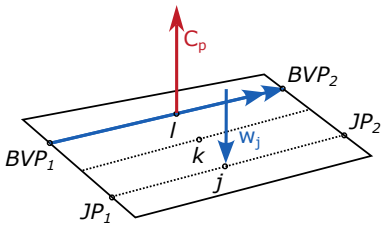

Fig. 5 Horseshoe Vortex DLM Panel.

the lifting force acting on the quarter line, w_j the downwash at the control point. The AIC matrices $Q_{jj}(k)$ capture both the added-mass and circulatory effects of unsteady aerodynamics. The complex-valued AIC matrix entry Q_{kl} can be thought of as an amplification of the sinusoidal input signal $w_l(t) = \|w_l\| \sin(\omega t)$ by $\|Q_{kl}\|$ and a phase shift by $\angle Q_{kl}$. In the limit as $k \to 0$, the unsteady solution smoothly converges to the quasi-steady solution provided by the Vortex Lattice Method. Importantly, the DLM solution $Q_{jj}(k)$ is a frequency-domain solution. Rational Function Approximation (RFA) is used to enable time-domain simulation and/or control design. The Doublet Lattice Method (DLM) provides unsteady aerodynamic influence coefficient (AIC) matrices $Q_{jj}(k)$ defined in the frequency domain, where k is the reduced frequency.

B. Rational Function Approximation

The DLM provides frequency-domain aerodynamic influence coefficients, which are incompatible with time-domain simulation and state-space control synthesis. To overcome this limitation, the frequency-dependent AIC matrices are approximated by rational functions in the Laplace variable, enabling conversion to an equivalent state-space representation with augmented aerodynamic lag states. This transformation is achieved using a Rational Function Approximation (RFA) technique, most commonly implemented via Roger's method[16, 20, 21]. Roger's method expresses the frequency-dependent AIC matrices $Q_{jj}(k)$ as a rational function in the Laplace domain. Introducing the normalized Laplace variable $s^* = s \cdot \left(\frac{c_{\text{ref}}}{2V_\infty}\right)$, the RFA takes the form

$$Q_{jj}(s^*) = Q_{jj}^{(0)} + Q_{jj}^{(1)} s^* + \sum_{i=1}^{n_p} Q_{jj}^{(L,i)} \frac{s^*}{s^* + p_i^*}, \tag{14}$$

where $Q_{jj}^{(0)}$ is the quasi-steady aerodynamics term; $Q_{jj}^{(1)}$ the added mass term; $Q_{jj}^{(L,i)}$ the lag term coefficients; and p_i^* the real, positive, dimensionless lag poles. This approximation introduces additional aerodynamic state variables, often called lag states, which evolve according to first-order differential equations of the form[16]:

$$\dot{x}_L = R_{LL} x_L + E_{Lj} \dot{w}_j, \tag{15}$$

where x_L are the lag states, R is a block-diagonal matrix with $-p_i I$ on the diagonal, and E couples the time derivative of the normal velocity $\dot{w}_j$ at the aerodynamic control points to the lag states[23]. The resulting unsteady aerodynamic pressure difference coefficients defined on the aerodynamic panel grid are

$$\Delta c_{p,j} = Q_{jj}^{(0)} w_j + \left(\frac{c_{\text{ref}}}{2V_\infty}\right) \left(Q_{jj}^{(1)} \dot{w}_j + D_{jL} x_L\right), \tag{16}$$

with D being the output matrix projecting lag states to aerodynamic forces. Importantly, this formulation allows a clear separation between steady w_j-dependent and unsteady $\dot{w}_j$-dependent contributions. In this aeroelastic modeling codebase the RFA is performed on the physical AIC matrices $Q_{jj}(k)$ prior to modal projection, preserving the physical interpretation and enabling consistent reuse across different structural configurations and mass cases. This avoids the mass-case-specific recomputation that generalized aerodynamic matrices would require. Figure 6 show exemplary Nyquist-Plots of the RFA of the rectangular wing's AIC matrices $Q_{jj}(k)$. The $200x200$ AIC matrix was evaluated at 12 reduced frequencies between 0 and 1.1, covering the frequency range up to 17.5 Hz, at the flutter-speed of 105 m/s, with flutter at roughly 4.5 Hz. In this example incompressible flow ($Ma = 0$) is assumed for simplicity. Extension to compressible flow aerodynamics is however straightforward. The number of distinct RFA poles was chosen to 6 which

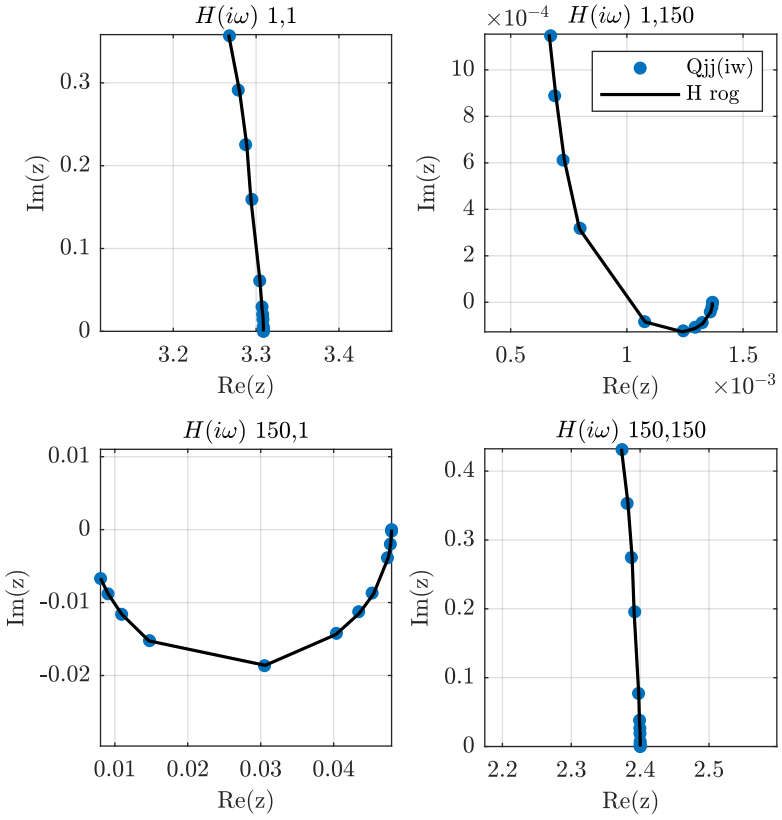

Fig. 6 Nyquist Plot of Rational Function Approximation AIC Matrices.

Table 1 Roger's Method RFA approximation errors

Max error worst frequency, worst matrix element	0.001818
RMS error all frequencies, worst matrix element	0.001002
RMS error all frequencies, all matrix elements	0.000113

results in $6 \cdot 200 = 1200$ aerodynamic lag states, if the pressure distribution on the lifting surface must be preserved. This illustrated the difficulty of aeroelastic modeling for control design. Even for the academic example of rectangular wing discretized with 200 aerodynamic panels the number of states in the linear model is enormous. In an industrial setting several thousand aerodynamic panels are typically necessary to capture the aerodynamics with sufficient accuracy. The error introduced by the RFA are evaluated at the reduced frequency reference points; see table 1. The Roger's RFA approximates the unsteady aerodynamic effects sufficiently well within the relevant frequency range.

IV. Coupling of Structural and Aerodynamic Model

In this work, aerodynamic loads are consistently projected onto the structural degrees of freedom of a beam-type finite element model. The projection is derived via the principle of virtual work, ensuring mechanical compatibility and energy consistency. Each aerodynamic panel generates a pressure force acting normal to the lifting surface, in the negative z-direction (lift). The integrated pressure force per panel P_i acts on the quarter point, located at $y = y_{P_i}$ with chordwise lever-arm x_{l,P_i}. The corresponding aerodynamic moment about the structural y-axis is for each panel

$$M_y(y_{P_i}) = a_{P_i} \cdot x_{l,P_i} \cdot C_{p,P_i}. \tag{17}$$

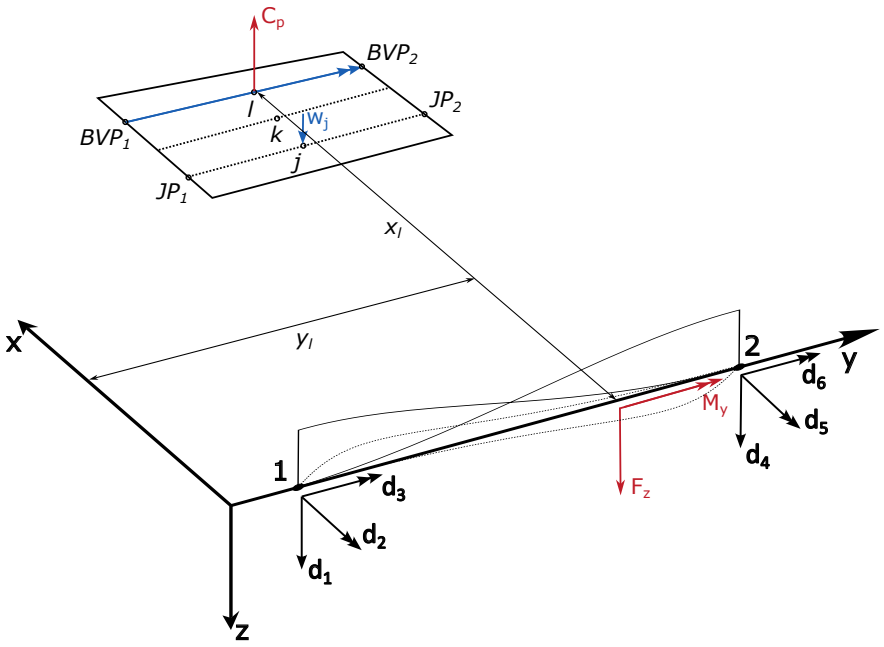

Fig. 7 Consistent Coupling of DLM and FEM.

Figure 7 illustrates the geometric relations between aerodynamic forces and the structural beam axis. The work done by the aerodynamic force on the structure is evaluated via the principle of virtual work:

$$\delta W_a = F_z \cdot \delta w_d, \tag{18}$$

where the total vertical displacement at the force application point includes both vertical translation and rotation:

$$w_d = u_z(y_{P_i}) + x_{l,P_i} \cdot \psi_y(y_{P_i}). \tag{19}$$

Thus, the virtual work becomes:

$$\delta W_a = -a_{P_i} C_{p,P_i} \left(\delta u_z(y_{P_i}) + x_{l,P_i} \cdot \delta\psi_y(y_{P_i})\right). \tag{20}$$

The structural displacements are interpolated via FEM shape functions at the spanwise location y_{P_i}

$$u_z(y_{P_i}) = \sum_i H_i(y_{P_i}) \cdot d_i; \qquad \psi_y(y_{P_i}) = \sum_i N_i(y_{P_i}) \cdot d_i, \tag{21}$$

where H_i are Hermite shape functions for bending, and N_i are linear shape functions for torsion. The total vertical displacement becomes

$$w_d = \sum_i H_i(y_{P_i}) \cdot d_i + x_{l,P_i} \sum_i N_i(y_{P_i}) \cdot d_i. \tag{22}$$

Substituting into the virtual work expression gives the consistent nodal force contributions

$$\delta W_a = \sum_i \left(-a_{P_i} C_{p,P_i} H_i(y_{P_i})\right) \delta d_i + \sum_i \left(-a_{P_i} C_{p,P_i} x_{l,P_i} N_i(y_{P_i})\right) \delta d_i. \tag{23}$$

Hence, the consistent external force vector from panel P_i is

$$F^{\text{ele}} = \begin{bmatrix} H_1(y_{P_i}) \cdot (-a_{P_i} C_{p,P_i}) \\ H_2(y_{P_i}) \cdot (-a_{P_i} C_{p,P_i}) \\ N_1(y_{P_i}) \cdot (-x_{l,P_i} \cdot a_{P_i} C_{p,P_i}) \\ H_3(y_{P_i}) \cdot (-a_{P_i} C_{p,P_i}) \\ H_4(y_{P_i}) \cdot (-a_{P_i} C_{p,P_i}) \\ N_2(y_{P_i}) \cdot (-x_{l,P_i} \cdot a_{P_i} C_{p,P_i}) \end{bmatrix}. \tag{24}$$

Summing over all aerodynamic panels, the global aerodynamic force vector acting on the structure is obtained as

$$F_g^{\text{aero}} = S_{gj} Q_{jj} w_j, \tag{25}$$

where Q_{jj} is the DLM influence matrix, w_j are the normal velocities at the control points, and S_{gj} is the consistent coupling matrix that maps aerodynamic forces to structural nodal forces using the above projection.

Conversely, the structural motion alters the boundary conditions of the flow through velocity compatibility at the aerodynamic control points. The generalized structural displacements q_g and their time derivatives $\dot{q}_g$ induce changes in the flow field, modeled as:

$$w_j = D_{jg}^{\text{Re}} q_g + D_{jg}^{\text{Im}} \dot{q}_g, \tag{26}$$

where D_{jg}^{Re}, D_{jg}^{Im} are coupling matrices formed by evaluating the shape functions at the control point locations. This projection ensures compatibility between the aerodynamic panel method and the structural FEM shape functions, preserving energy consistency. Consequently, approximate spline interpolation is unnecessary.

V. Actuator and Sensor Models

The generic rectangular wing model developed in this work is equipped with four leading edge slats and four trailing edge flaps of equal dimension, covering the entire span of the wing. The chordwise size of each control surface is 1/10 of the total chord length, modeled by first and last row of the DLM panel discretization for slats and flaps, respectively. Figure 8 shows the full aerodynamic panel discretization. Notice the chordwise first and last panels are used to model trailing edge flaps and leading edge slats. The red dots indicate the position of the vertical acceleration sensors. Accurate representation of actuator dynamics is essential for aeroservoelastic controller design, as unmodeled phase

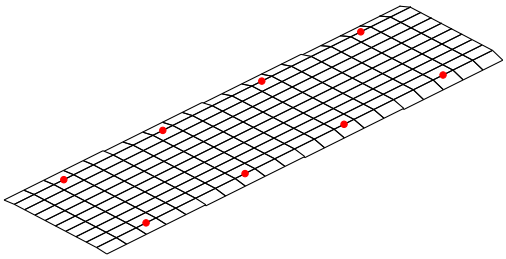

Fig. 8 Unsteady Aerodynamic DLM Panel Discretization.

loss in the control path can significantly degrade stability margins. Typical control surface deflection servos introduce non-negligible phase lag due to the high frequency nature of flutter suppression[12]. To represent the dynamics of the control effector, a second-order low-pass filter (PT2) was selected.

$$G_{\text{act}}(s) = \frac{K\omega_0^2}{s^2 + 2d\omega_0 s + \omega_0^2}, \tag{27}$$

with parameters $K = 1$, damping ratio $d = 1$, and natural frequency $\omega_0 = 2\pi \cdot 16$ rad/s, corresponding to a -3 dB bandwidth of approximately 10 Hz. This choice ensures sufficient responsiveness for active flutter suppression, as the first aeroelastic mode of the system becomes unstable around 4.5 Hz. A PT2 actuator model was chosen over a simpler first-order (PT1) model due to the nature of the aerodynamic model. Specifically, the unsteady aerodynamic forces depend not only on the position of the control surface but also on its velocity and acceleration. In the Simulink implementation of the benchmark wing system, actuator saturation limits and rate limits were also included to reflect realistic constraints of typical servo actuators. These nonlinearities are essential for evaluating the robustness and performance of active flutter suppression controllers under realistic operational limits and for enabling safe deployment scenarios in simulation-based controller validation.

The model includes eight distributed vertical acceleration measurements. In practice local acceleration can be measured cost efficient using standard Inertial Measurement Units (IMUs). These sensors are intended to capture the

structural dynamics relevant to aeroelastic instabilities. The models local acceleration measurement outputs are given by

$$a_z = \Phi_{zg}\, \ddot{q}_g \ , \tag{28}$$

where Φ_{zg} maps generalized accelerations $\ddot{q}_g$ to the respective sensor positions.

VI. Linear Parameter Varying State Space Model

Finally the structural dynamic equation of motion 12 is combined with the aerodynamic force vector 25. The AIC Matrix term Q_{jj} is substituted with its Rational Function Approximation 16 and the local downwash at the aerodynamic control points w_j with its contributions from the dynamic deformation of the structure 26 as well as control surface deflection. Expressed in Structural FEM DoFs the full equation of motion reads

$$M_{gg}s^2 q_g + D_{gg}sq_g + K_{gg}q_g = \left(Q_{jj}^{(0)} + Q_{jj}^{(1)}s^* + \sum_{i=1}^{n_p} Q_{jj}^{(L,i)} \frac{s^*}{s^* + p_i}\right) \cdot \left(D_{jg}^{\mathrm{Re}} q_g + D_{jg}^{\mathrm{Im}} \dot{q}_g + D_{jx}^{\mathrm{Re}} u_x + D_{jx}^{\mathrm{Im}} \dot{u}_x\right). \tag{29}$$

This is a linear equation of motion and may be cast into a first-order state-space form

$$\dot{\mathbf{x}} = \mathbf{A}(V_\infty)\mathbf{x} + \mathbf{B}(V_\infty)\mathbf{u}, \quad \mathbf{y} = \mathbf{C}(V_\infty)\mathbf{x} + \mathbf{D}(V_\infty)\mathbf{u} \tag{30}$$

where the system matrices depend explicitly on the freestream velocity V_∞, rendering the model a linear parameter-varying (LPV) system. The state vector $\mathbf{x}$ includes both structural and aerodynamic states. The transformation of eq. 29 into state space form shall be discussed in the following. Key definitions are repeated for convenience:

- **Dynamic pressure:**

$$\bar{q} = \frac{1}{2}\rho V_\infty^2, \tag{31}$$

- **Reduced frequency:**

$$k = \omega \frac{c_{ref}}{2V_\infty}, \tag{32}$$

- **Dimensionless Laplace variable:**

$$s^* = s \frac{c_{ref}}{2V_\infty}, \tag{33}$$

- **RFA lag poles:**

$$p_i = p_i^* \frac{2V_\infty}{c_{ref}} \ . \tag{34}$$

Transformation of the Second-Order Structural Dynamics The structural dynamic from the beam FE model is a second-order linear differential equation

$$M_{gg}\ddot{q}_g + D_{gg}\dot{q}_g + K_{gg}q_g = F_g^{\mathrm{aero}} \ . \tag{35}$$

Here, q_g denotes the structural coordinates (FEM DoFs). To express this in state-space form, we define the structural state vector $\mathbf{x_s} = \begin{bmatrix} q_g \\ \dot{q}_g \end{bmatrix}$,

$$\begin{bmatrix} \dot{q}_g \\ \ddot{q}_g \end{bmatrix} = \begin{bmatrix} 0 & I \\ -M_{gg}^{-1}K_{gg} & -M_{gg}^{-1}D_{gg} \end{bmatrix} \begin{bmatrix} q_g \\ \dot{q}_g \end{bmatrix} + \begin{bmatrix} 0 \\ M_{gg}^{-1} \end{bmatrix} F_g^{\mathrm{aero}} \tag{36}$$

Inclusion of Aerodynamic Lag States The unsteady aerodynamic forces computed via the Doublet Lattice Method (DLM) are approximated in the Laplace domain using Roger's Rational Function Approximation (RFA), which introduces first-order lag dynamics:

$$\dot{x}_L = R_{LL}x_L + E_{Lj}\dot{w}_j \tag{37}$$

where x_L are the aerodynamic lag states and w_j are the downwash velocities at the DLM control points. These depend on both structural velocities and control surface motions. The lag states capture the aerodynamic memory effects and enable an accurate time-domain representation. The aerodynamic forces are reconstructed as:

$$F_g^{\mathrm{aero}} = \bar{q}S_{gj}\left(Q_{jj}^{(0)}w_j + \left(\frac{c_{ref}}{2V_\infty}\right)Q_{jj}^{(1)}\dot{w}_j + D_{jL}x_L\right) \tag{38}$$

Final Coupled State-Space Form Combining the structural and aerodynamic dynamics, the complete state vector becomes:

$$\mathbf{x} = \begin{bmatrix} q_g \\ \dot{q}_g \\ x_L \end{bmatrix} \tag{39}$$

The respective first-order LPV state-space system reads:

$$\begin{bmatrix} \dot{q}_g \\ \ddot{q}_g \\ \dot{x}_L \end{bmatrix} = \begin{bmatrix} 0_{gg} & I_{gg} & 0_{gL} \\ \tilde{M}_{gg}^{-1}\tilde{K}_{gg} & \tilde{M}_{gg}^{-1}\tilde{D}_{gg} & \tilde{M}_{gg}^{-1}D_{gL} \\ E_{Lg} & 0_{Lg} & R_{LL} \end{bmatrix} \begin{bmatrix} q_g \\ \dot{q}_g \\ x_L \end{bmatrix} + \begin{bmatrix} 0_{gx} & 0_{g\dot{x}} & 0_{g\ddot{x}} \\ \tilde{M}_{gg}^{-1}B_{gx} & \tilde{M}_{gg}^{-1}B_{g\dot{x}} & \tilde{M}_{gg}^{-1}B_{g\ddot{x}} \\ E_{Lx} & 0_{L\dot{x}} & 0_{L\ddot{x}} \end{bmatrix} \begin{bmatrix} u_x \\ \dot{u}_x \\ \ddot{u}_x \end{bmatrix} \tag{40}$$

This state space formulation ensures compatibility with modern control synthesis. The matrix entries are defined in the appendix.

Output Equation The measurement model provides the vertical accelerations a_z of distributed points on the wing,

$$a_z = \Phi_{zg}\, \ddot{q}_g \ , \tag{41}$$

i.e. a linear mapping from the structural coordinates second time derivative (structural accelerations $\ddot{q}_g$. Since the structural acceleration appears on the left side of the final state space dynamic equation 40, the full system dynamics are repeated in the output equation

$$\mathbf{y} = \mathbf{C}\mathbf{x} + \mathbf{D}\mathbf{u} \ . \tag{42}$$

Which explained the intuitively nonphysical artifact of feed-through term $\mathbf{D}$ in the benchmark wings state space model.

$$a_z = \begin{bmatrix} \Phi_{zg}\tilde{M}_{gg}^{-1}\tilde{K}_{gg} & \Phi_{zg}\tilde{M}_{gg}^{-1}\tilde{D}_{gg} & \Phi_{zg}\tilde{M}_{gg}^{-1}D_{gL} \end{bmatrix} \begin{bmatrix} q_g \\ \dot{q}_g \\ x_L \end{bmatrix} + \begin{bmatrix} \Phi_{az}\tilde{M}_{gg}^{-1}B_{gx} & \Phi_{az}\tilde{M}_{gg}^{-1}\tilde{B}_{g\dot{x}} & \Phi_{az}\tilde{M}_{gg}^{-1}\tilde{B}_{g\ddot{x}} \end{bmatrix} \begin{bmatrix} u_x \\ \dot{u}_x \\ \ddot{u}_x \end{bmatrix} \tag{43}$$

Modal Projection The finite element discretization described in Section II results in a potentially very high-dimensional system. In fact the number aerodynamic lag states is number of aero panels n_j times number of Roger's poles n_p, and the number of structural states is twice the FEM DoFs n_g. In total the number of states $n_S = 2n_q + n_p n_j$ is in general prohibitively large for any controller synthesis method. Even this comparatively very lightweight benchmark model yields a total number of $n_S = 2 \cdot 51 + 6 \cdot 200 = 1302$ system states. To render the system computationally tractable for control synthesis and to filter very high frequency dynamics irrelevant to the flutter phenomenon, a modal reduction is performed. This process projects the physical dynamics onto a truncated set of the structure's dominant eigenmodes. The undamped natural modes of vibration are obtained by solving the generalized eigenvalue problem associated with the conservative structural system

$$M_{gg}\ddot{q}_g + K_{gg}q_g = 0 \ . \tag{44}$$

The corresponding generalized eigenvalue problem

$$(K_{gg} - \omega_r^2 M_{gg})\phi_r = 0, \quad r = 1, \ldots, n_g \tag{45}$$

is solved for the positive eigenfrequencies ω_r and the associated mass-orthonormal mode shapes ϕ_r, satisfying

$$\Phi_{gf}^\top M_{gg}\Phi_{gf} = I_f, \quad \Phi_{gf}^\top K_{gg}\Phi_{gf} = \mathrm{diag}(\omega_r^2). \tag{46}$$

Mass-normalization reduces ill-conditioning that commonly arises for large unscaled FE models. Here $\Phi_{gf} \in \mathbb{C}^{n_g \times n_f}$ contains the $n_f \ll n_g$ retained modes (typically the lowest 5 modes), and the subscript f denotes the modal (flexible) coordinate system.

$$\Phi_{gf} = \left[\phi_1, \phi_2, \ldots, \phi_{n_f}\right]. \tag{47}$$

The structural displacements and velocities are then approximated as

$$q_g(t) = \Phi_{gf}q_f(t), \quad \dot{q}_g(t) = \Phi_{gf}\dot{q}_f(t), \tag{48}$$

where $q_f \in \mathbb{R}^{n_f}$ are the modal coordinates. Substituting into the structural equation of motion (12) and pre-multiplying by $\Phi_{gf}^\top$ yields the modal form

$$\underbrace{\Phi_{gf}^\top M_{gg} \Phi_{gf}}_{=I_f} \ddot{q}_f + \underbrace{\Phi_{gf}^\top K_{gg} \Phi_{gf}}_{=\mathrm{diag}(\omega_r^2)} q_f = \Phi_{gf}^\top F_g^{\mathrm{aero}}. \tag{49}$$

The generalized aerodynamic forces, coupling matrices, and downwash contributions are projected accordingly:

$$S_{fj} = \Phi_{gf}^\top S_{gj} \in \mathbb{R}^{n_f \times n_j}, \tag{50}$$

$$D_{jf}^{\mathrm{Re}} = D_{jg}^{\mathrm{Re}} \Phi_{gf} \in \mathbb{R}^{n_j \times n_f}, \tag{51}$$

$$D_{jf}^{\mathrm{Im}} = D_{jg}^{\mathrm{Im}} \Phi_{gf} \in \mathbb{R}^{n_j \times n_f}. \tag{52}$$

Note that actuator and sensor mappings must be transformed in the same manner, e.g. $\Phi_{zg} \mapsto \Phi_{zf} = \Phi_{zg}\Phi_{gf}$. Additionally, the modal projection allows empirical structural damping to be introduced. In this work viscous modal damping is assumed for simplicity. A viscous modal damping matrix D_{ff} is constructed assuming a constant damping ratio ζ for all retained modes:

$$D_{ff} = \mathrm{diag}(2\zeta_r \omega_r), \tag{53}$$

with a uniform damping ratio $\zeta_r = 0.01$ applied to all retained modes.

A significant reduction in system states is achieved by projecting the lag state dynamics of eq. 37 onto the retained structural modes. After some tedious algebraic manipulations the projected aerodynamic modal forces become

$$\begin{aligned}
F_f^{\mathrm{aero}} = \bar{q} S_{fj} &\left(Q_{jj}^0 D_{jf}^{Re} + \sum_{i=1}^{n_p} Q_{jj}^{L_i} (D_{jf}^{Re} - p_i \frac{1}{V_\infty} D_{jf}^{Im}) \right) && \cdot q_f \\
+ \bar{q} S_{fj} &\left(Q_{jj}^0 \frac{1}{V_\infty} D_{jf}^{Im} + Q_{jj}^1 \frac{c_{ref}}{2V_\infty} D_{jf}^{Re} + \sum_{i=1}^{n_p} Q_{jj}^{L_i} \frac{1}{V_\infty} D_{jf}^{Im} \right) && \cdot s q_f \\
+ \bar{q} S_{fj} &\left(Q_{jj}^1 \frac{c_{ref}}{2V_\infty} D_{jf}^{Im} \right) && \cdot s^2 q_f \\
+ \bar{q} S_{fj} &\sum_{i=1}^{n_p} Q_{jj}^{L_i} \frac{(\frac{1}{V_\infty} D_{jf}^{Im} p_i^2 - D_{jf}^{Re} p_i)}{s + p_i} && \cdot q_f \ .
\end{aligned} \tag{54}$$

The respective terms of eq. 54 are aerodynamic stiffness, damping, mass and lag. With the aerodynamic forces projected onto the retained modeshapes the total number of system states becomes $n_S = 2n_f + n_f n_p$. With 5 retained structural modes and 6 RFA poles for this benchmark model $x_S = 40$. Note the additional 2 states introduced by each actuator. An equivalent state space form, suitable for implementation, of the lag term of Eq. (54) can be found in the appendix in Eq. 72. The generalized modal forces remain fully representative of the physical system, making this reduced-order model ideal for control synthesis. Modal projection introduces several important limitations that must be acknowledged.

First, projecting aerodynamic forces through a modal basis compresses the distributed pressure field into modal generalized forces, resulting in loss of spatial pressure detail. Consequently, quantities requiring local pressure information, such as panel-level hinge moments, cannot be recovered from the truncated modal model.

Second, the validity of the reduced model depends critically on selecting modes that capture the dynamic energy in the frequency band of interest. Modal truncation that omits modes having non-negligible aerodynamic coupling can produce erroneous predictions of flutter speed and modal damping. A pragmatic selection criterion is to include all modes with eigenfrequencies up to two to three times the expected flutter frequency.

Third, model reduction should be accompanied by quantitative error metrics such as the reconstruction error $\|q_g - \Phi_{gf} q_f\|$ and the discrepancy in computed eigenvalues between full and reduced models; however, such analysis was beyond the scope of this work.

VII. Modal Analysis

A fundamental analysis step is the modal decomposition of the system, which facilitates physical insight into the dominant mechanisms of instability such as flutter or divergence. Consider the linear state space dynamics

$$\dot{x}(t) = Ax(t), \quad x \in \mathbb{R}^n \ . \tag{55}$$

The modal transformation is a similarity transformation that diagonalizes the system matrix A into a set of decoupled modes:

$$x = Tz \quad \Rightarrow \quad \dot{z} = T^{-1}ATz = \Lambda z \tag{56}$$

This modal transformation of the full aeroelastic model must not be confused with the modal projection onto the dominant modes of the conservative structural system in sec. VI. The coupled structural-aerodynamic system exhibits characteristic aeroelastic behavior due to the interaction between aerodynamic and structural forces. Two critical aeroelastic modes dominate the benchmark rectangular wing's system dynamics near the instability boundary. These modes manifest around a frequency of 4.5 Hz, corresponding to a circular frequency of approximately 28 rad/s, and are responsible for the onset of bending-torsion flutter. Figure 9 depicts the deflection of the bending and the torsion structural mode for a full oscillation of the fluttermode at flutter speed. Note the typical phase shift between bending and torsion. The structural mode deflections are scaled to be energy equivalent. That is a static bending deformation of amplitude 1 stores the same amount of elastic potential energy as a torsion amplitude of 1. The bending-torsion fluttermode of the benchmark wing is thus dominated by bending.

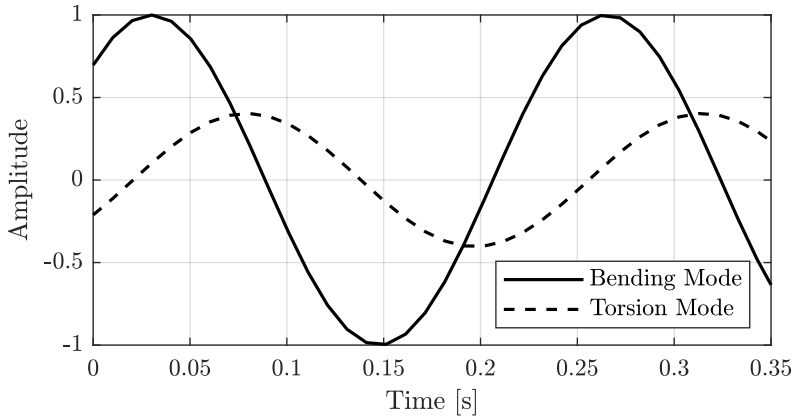

Fig. 9 Full Period of Flutter Bending & Torsion

Modal Characteristics at Fixed Velocities To illustrate the evolution of the aeroelastic poles, Fig. 10 shows the pole locations of the linear time-invariant (LTI) system linearized at two representative freestream velocities. At a subcritical velocity of $V_\infty = 60$ m/s, the system is stable and all poles lie in the left-half complex plane (Fig. 10a). The two critical aeroelastic modes are visible near the imaginary axis with low damping and dominant imaginary parts around 28 rad/s. As the velocity increases to $V_\infty = 120$ m/s (Fig. 10b), the damping of these modes reduces further, and one pair of complex conjugate poles crosses into the right-half plane, signaling the onset of flutter instability.

Classical Flutter Characteristics The velocity-dependent evolution of modal frequency and damping is depicted in the classical flutter plots[24] shown in Figure 11. The top plot illustrates the frequency ($V\omega$-plot), and the bottom plot shows the corresponding damping ratios (Vg-plot) of the two critical modes as functions of freestream velocity. A distinct coalescence and subsequent divergence of the mode pair is observed, culminating in the flutter boundary where the damping becomes zero. This intersection occurs at a critical flutter speed around 105 m/s.

LPV Pole Trajectory with Velocity The complete trajectory of the aeroelastic eigenvalues as a function of freestream velocity is shown in the colored pole map in Figure 12. This visualization highlights the continuous motion of poles in the complex plane as V_∞ increases. Initially, the two dominant modes are well separated, but they gradually converge and couple due to increasing aerodynamic interaction. Eventually, one pair becomes unstable beyond the critical flutter speed, consistent with the observations from the flutter plots.

Structural Composition of Critical Modes To further analyze the physical nature of the two critical aeroelastic modes, their eigenvectors are projected onto the structural degrees of freedom and evaluated as functions of freestream

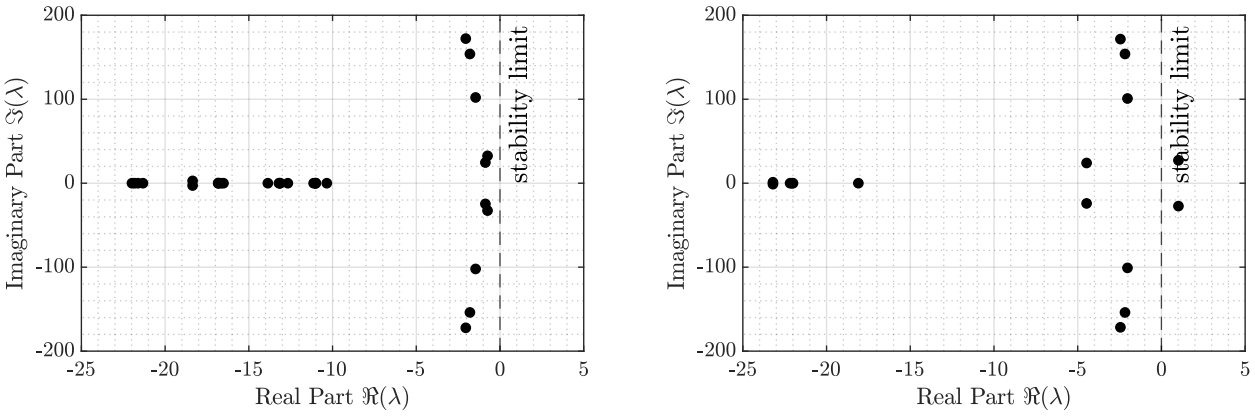

(a) Pole Map at Velocity below Flutter

(b) Pole Map at Velocity in Flutter Region

Fig. 10 Pole Maps in Stable and Unstable Regime

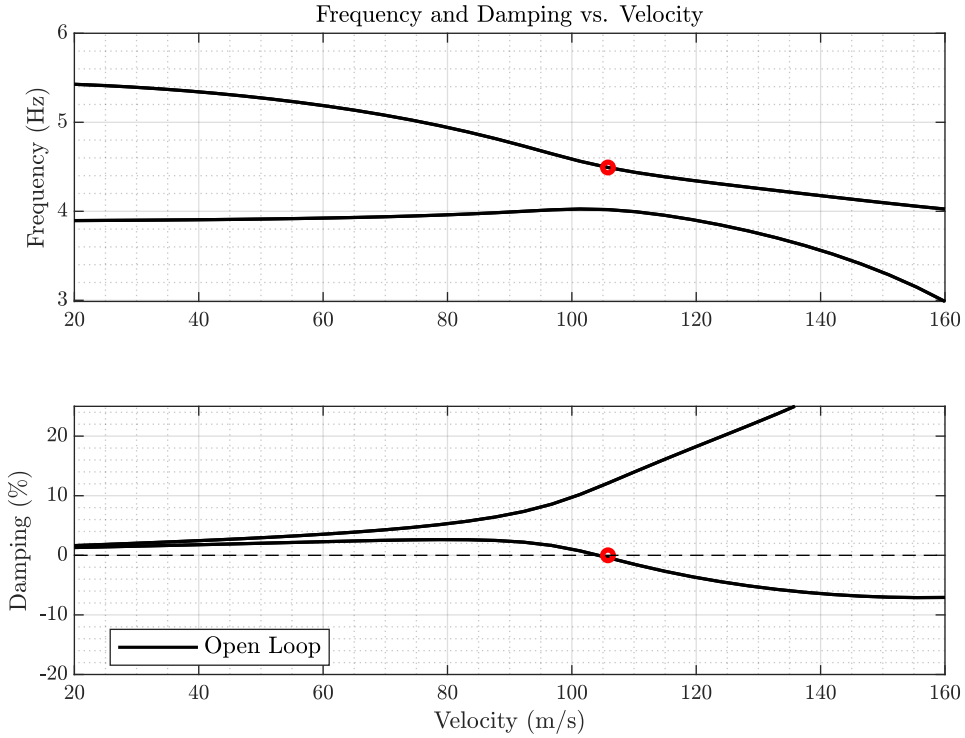

Fig. 11 Vg-Plot and $V\omega$-Plot of Rectangular Wing

velocity. Figure 13 plots the relative magnitude of bending and torsion components of the modal shapes across velocities. At low velocities (e.g., 20 m/s), the two modes are largely uncoupled: one mode is dominated by bending, the other by torsion. However, as velocity increases, the eigenvectors become increasingly aligned, indicating strong coupling between bending and torsional dynamics[25]. This alignment is evident in the convergence of their respective projections, reflecting a coalescence in both frequency and modal content. Near and beyond the flutter boundary, both modes exhibit nearly collinear structural components, underscoring the mixed bending-torsion character of the unstable flutter mode. This modal evolution provides insight into the physical mechanisms leading to instability and motivates the selection of sensor and actuator placements that target these specific dynamics. Moreover, the velocity-dependent nature of the system justifies the use of a linear parameter-varying (LPV) framework for active flutter suppression,

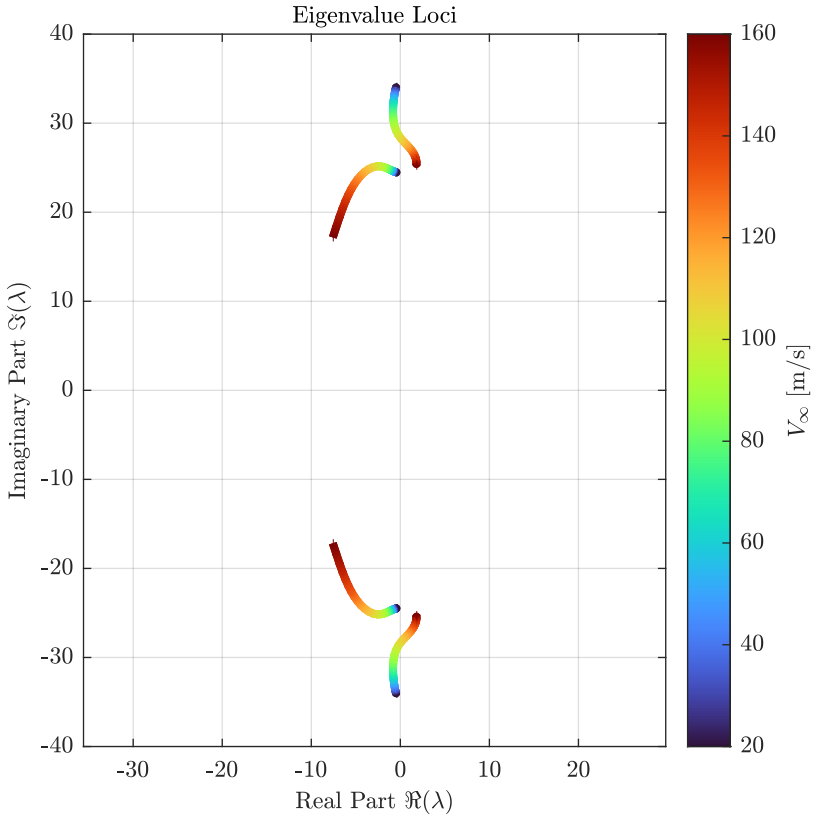

Fig. 12 Pole-Map of Rectangular Wing

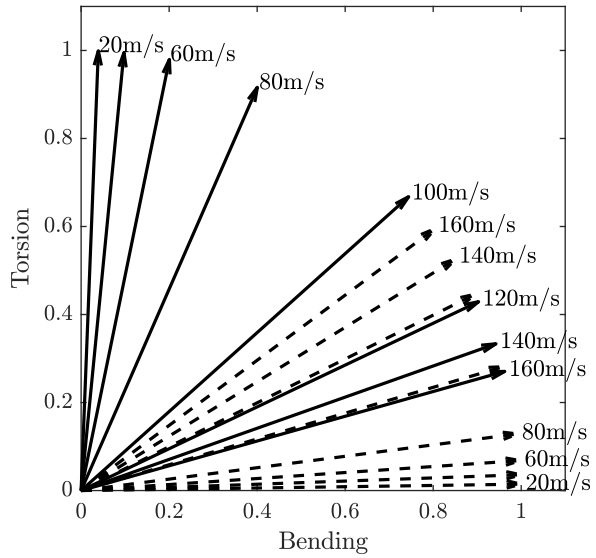

Fig. 13 Bending and Torsion Components of Critical Modes over V_∞

enabling robust control strategies to stabilize the critical modes across the operating envelope.

Modal Observability & Controllability Measures For a real eigenvalue with individually normalized eigenvectors satisfying $\|v_i\| = \|w_i\| = 1$ (as opposed to bi-orthonormalization $w_i^H v_j = \delta_{ij}$), suitable scalar measures of modal controllability and observability are given by

$$|h_i| = \|Cv_i\|, \tag{57}$$

$$|f_i| = \left\|w_i^H B\right\|, \tag{58}$$

where $|h_i|$ represents the effective observability of mode i across all outputs, and $|f_i|$ the effective controllability of mode i via all inputs [26]. For complex conjugate eigenvalues $\lambda_i = \delta \pm i\omega$, the same procedure applies, where $\|\Re\{Cv_i\}\|$ reflects observability of the modal "damping" $\Re\{\lambda_i\}$, and $\|\Im\{Cv_i\}\|$ reflects observability of the modal "frequency" $\Im\{\lambda_i\}$. Dually $\left\|\Re\{w_i^H B\}\right\|$ reflects controllability of the modal "damping" $\Re\{\lambda_i\}$, and $\left\|\Im\{w_i^H B\}\right\|$ reflects controllability of the modal frequency $\Im\{\lambda_i\}$.

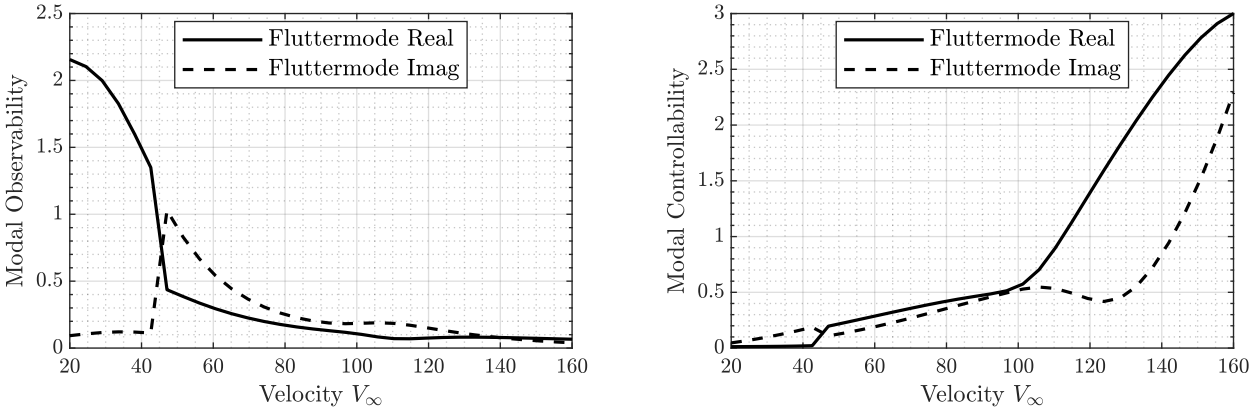

(a) Flutter Observability **(b) Flutter Controllability**

Fig. 14 Flutter Modal Observability & Controllability

Figure 14 depicts the evolution of flutter modal observability & controllability over freestream velocity. The absolute numerical value is of lesser importance as system state and output are scaled for numerical stability. Counterintuitively the flutter mode seems to be most observable at low frequencies. Between 20 and 60 m/s, observability decreases sharply; thereafter, it degrades more gradually. This phenomenon can be explained by the normalization of the modeshape vector v_i, where at low airspeeds the flutter mode is dominated by the measurable structural deformation states $(q_f, \dot{q}_f)$. At high airspeeds the fluttermode is increasingly dominated by non measurable aerodynamic lag states, therefore, the apparent observability of the normalized eigenvector decreases. Time simulation however confirms that actual acceleration measurements, of course, increase sharply around the onset of the flutter instability.

As one would expect the fluttermode is increasingly well controllable as freestream velocity grows. Since the effectivity of aerodynamic control surfaces grows linearly with the dynamic pressure $\bar{q}$, i.e. quadratically with V_∞. Note that increasing controllability in the sense of Eq. (57) refers solely to the amount of energy introduced to the fluttermode by a unit system input. In fact intuitive "controllability", i.e. keeping the system at a desirable state through feedback, is, of course, increasingly difficult with an increasingly unstable flutter pole pair. [27]

In summary, the flutter mode of the generic rectangular wing is reasonably measurable from eight distributed vertical acceleration sensors and sufficiently controllable with 4 leading edge slats and 4 trailing edge flaps covering the full wing span. In fact a singe outboard aileron (trailing edge flap) may be sufficient for active flutter suppression, as demonstrated in the following section VIII.

VIII. Active Flutter Suppression

To demonstrate the practical application of the proposed benchmark model for control design, a simple active flutter suppression controller similar to the approach by Horikawa and Dowell[28] is implemented. The controller is based

on constant output feedback[29] using measurements from the two outermost acceleration sensors and actuating only the outboard trailing-edge aileron. A proportional output feedback strategy is employed, which stabilizes the system

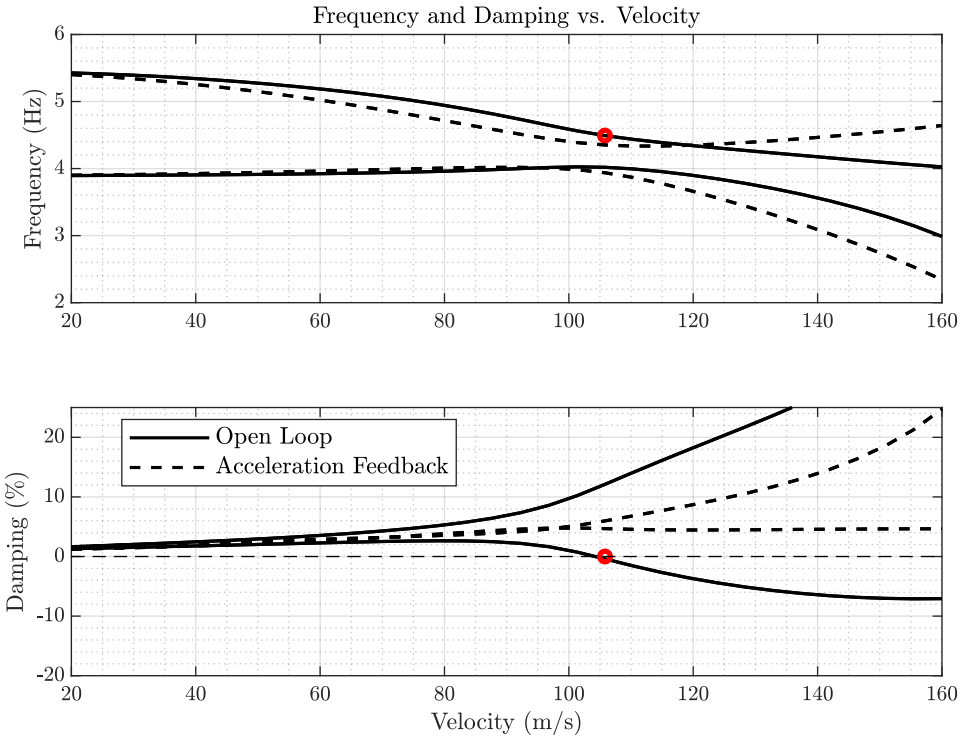

Fig. 15 Vg-Plot and $V\omega$-Plot of Open Loop vs. Acceleration Feedback

across a range of freestream velocities. This approach illustrates how even a minimal control architecture can shift the flutter boundary and increase modal damping. The effectiveness of this setup is illustrated in Fig. 15, which compares the velocity-dependent damping and frequency characteristics (V_g and V_ω plots) for the open-loop and closed-loop systems. The corresponding pole trajectories in the complex plane are shown in Fig. 16, indicating the stabilizing shift of the unstable flutter poles under feedback control. This example serves as a first proof-of-concept for active flutter suppression using the benchmark model. It highlights that stabilizing control can be achieved with surprisingly simple static feedback control. However, no considerations have been made regarding the robustness of this control strategy to modeling uncertainties. Additionally, nonlinear actuator limitations such as saturation,and rate constraints have been neglected. These factors are critical in real-world applications and must be addressed in more advanced designs[2]. Nonetheless, this example showcases the utility of the benchmark for validating fundamental controller concepts and provides a basis for the development of more sophisticated control strategies, including robust and gain-scheduled approaches. The author presents a refined active flutter suppression controller in a companion work [30].

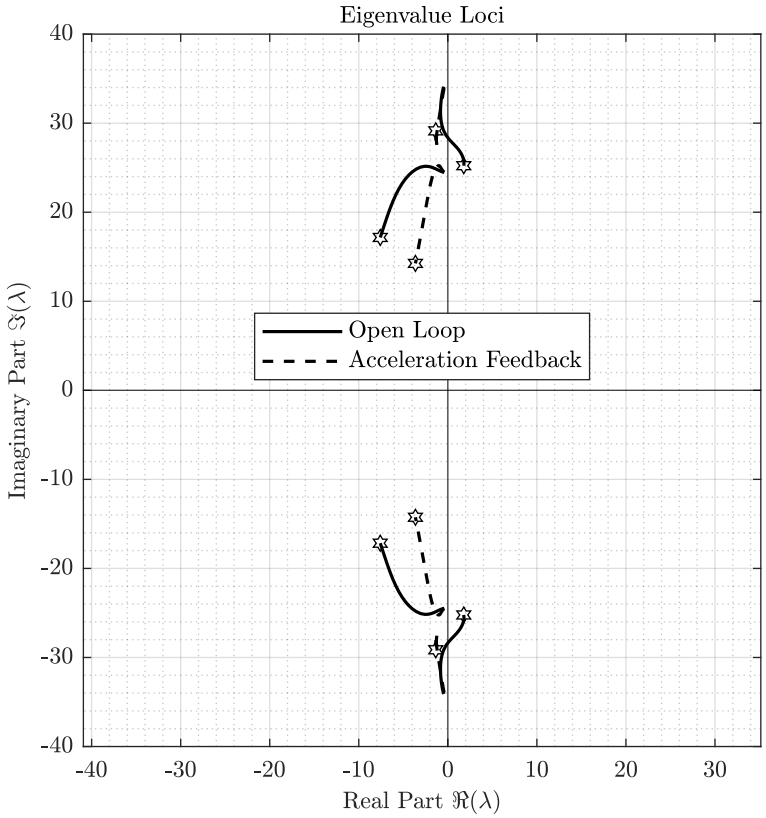

Fig. 16 Pole-Map of Open Loop vs. Acceleration Feedback

IX. Conclusion

This paper presents a complete, yet comprehensible open-source benchmark model designed to support the development and evaluation of secondary flight control strategies. The model integrates a finite element (FE) beam representation of a flexible wing structure with unsteady aerodynamic loading derived from the Doublet Lattice Method (DLM). Structural and aerodynamic model are consistently coupled without approximate spline interpolation. The frequency domain DLM is converted to the time-domain via Rational Function Approximation (RFA) using Roger's method. This formulation results in a Linear Parameter-Varying (LPV) state-space model dependent on the freestream velocity, facilitating modern control synthesis techniques.

A key strength of the benchmark lies in its balance between physical fidelity and computational tractability. The structural model captures the fundamental bending and torsional dynamics of a high-aspect-ratio wing. The unsteady aerodynamic effects are modeled using the industry standard linearized potential flow panel method instead of 2-D Theodorsen theory commonly used in research. The actuator layout, consisting of trailing edge flaps and leading edge slats, along with the distributed inertial sensors reflects possible future flight control configurations. Standard PT2 actuator dynamics as well as generic sensor noise are taken into account. This enables the rapid design and testing of control strategies under representative conditions.

The benchmark includes a detailed modal analysis of the coupled aeroservoelastic system, enabling the tracking of eigenvalue trajectories as a function of airspeed. The transition from stable to unstable regimes is clearly characterized, revealing the physical mechanisms underlying classical bending torsion flutter onset. Additionally, velocity-dependent assessments of modal controllability and observability provide insight into the effectiveness of different sensor-actuator combinations, informing control design decisions.

Overall, the proposed benchmark bridges the methodological gap between the high-fidelity aeroelastic models used in industry and simplistic 2-D airfoil formulations dominating control research. It provides a reproducible platform for rigorous testing of novel active flutter suppression and/or gust/maneuver load alleviation strategies and encourages

systematic performance comparisons across competing methodologies. Future extensions of this work may include the incorporation of parameter uncertainty, extension to a 3-D truss type airframe model and rigid body dynamics.

The accompanying MATLAB/Simulink implementation provides a extensible, and transparent environment for simulation, controller design, and performance evaluation. The respective code is available at github.com/JonasEiche/FlutterWing.

Appendix

Key variables used in sec. VI are defined below.

q_g	=	structural coordinates (FEM DoFs)
q_f	=	modal coordinates (flexible)
u_x	=	control surface deflections
x_L	=	aerodynamic lag states
F_g^{aero}	=	aerodynamic force vector
M_{gg}	=	structural mass matrix
D_{gg}	=	structural damping matrix
K_{gg}	=	structural stiffness matrix
S_{gj}	=	aero force integration
$Q_{jj}(s^*)$	=	AIC matrix
$Q_{jj}^{(0)}$	=	quasi-steady AIC term
$Q_{jj}^{(1)}$	=	added mass AIC term
$Q_{jj}^{(L,i)}$	=	aerodynamic lag AIC coefficients
D_{jg}^{Re}	=	struct def. to downwash map
D_{jg}^{Im}	=	struct vel. to downwash map
D_{jx}^{Re}	=	cs deflection to downwash map
D_{jx}^{Im}	=	cs deflection vel. to downwash map
R_{LL}	=	lag state dynamics matrix ($\simeq A$)
E_{Lj}	=	lag state aero input matrix ($\simeq B$)
D_{jL}	=	lag state aero output matrix ($\simeq C$)
E_{Lg}	=	lag state struct input matrix ($\simeq B$)
E_{Lx}	=	lag state cs input matrix ($\simeq B$)
D_{gL}	=	lag state struct output matrix ($\simeq C$)

$$\tilde{M}_{gg} = M_{gg} - \bar{q} S_{gj} Q_{jj}^{(1)} \frac{c_{ref}}{2V_\infty} \frac{1}{V_\infty} D_{jg}^{Im} \tag{59}$$

$$\tilde{D}_{gg} = -D_{gg} + \bar{q} S_{gj} \left(Q_{jj}^{(0)} \frac{1}{V_\infty} D_{jg}^{Im} + Q_{jj}^{(1)} \frac{c_{ref}}{2V_\infty} D_{jg}^{Re} + \sum_{i=1}^{n_p} Q_{lj}^{L_i} \frac{1}{V_\infty} D_{jg}^{Im} \right) \tag{60}$$

$$\tilde{K}_{gg} = -K_{gg} + \bar{q} S_{gj} \left(Q_{jj}^{(0)} D_{jg}^{Re} + \sum_{i=1}^{n_p} Q_{jj}^{(L_i)} \left(D_{jg}^{Re} - p_i \frac{1}{V_\infty} D_{jg}^{Im} \right) \right) \tag{61}$$

$$B_{gx} = \bar{q} S_{gj} Q_{ij}^{j} \left(Q_{jj}^{(0)} D_{jx}^{Re} + \sum_{i=1}^{n_p} Q_{jj}^{(L_i)} \left(D_{jx}^{Re} - p_i \frac{1}{V_\infty} D_{jx}^{Im} \right) \right) \tag{62}$$

$$B_{g\dot{x}} = \bar{q} S_{gj} \left(Q_{jj}^{(0)} \frac{1}{V_\infty} D_{jx}^{Im} + Q_{jj}^{(1)} \frac{c_{ref}}{2V_\infty} D_{jx}^{Re} + \sum_{i=1}^{n_p} Q_{jj}^{(L_i)} \frac{1}{V_\infty} D_{jx}^{Im} \right) \tag{63}$$

$$B_{g\ddot{x}} = \bar{q} S_{gj} Q_{jj}^{(1)} \frac{c_{ref}}{2V_\infty} \frac{1}{V_\infty} D_{jx}^{Im} \tag{64}$$

$$\tag{65}$$

$$R_{LL} = \begin{bmatrix} -p_1 I_{jj} & & \\ & \ddots & \\ & & -p_{n_p} I_{jj} \end{bmatrix} \tag{66}$$

$$E_{Lj} = \begin{bmatrix} Q_{jj}^{(L_1)} \\ \vdots \\ Q_{jj}^{(L_{n_p})} \end{bmatrix} \tag{67}$$

$$E_{Lg} = \begin{bmatrix} Q_{jj}^{(L_1)} (\frac{1}{V_\infty} D_{jg}^{Im} p_1^2 - D_{jg}^{Re} p_1) \\ \vdots \\ Q_{jj}^{(L_{n_p})} (\frac{1}{V_\infty} D_{jg}^{Im} p_{n_p}^2 - D_{jg}^{Re} p_{n_p}) \end{bmatrix} \tag{68}$$

$$D_{gL} = \bar{q} \left[S_{gj}, ..., S_{gj} \right] \tag{69}$$

$$E_{Lx} = \begin{bmatrix} Q_{jj}^{(L_1)} (\frac{1}{V_\infty} D_{jx}^{Im} p_1^2 - D_{jx}^{Re} p_1) \\ \vdots \\ Q_{jj}^{(L_{n_p})} (\frac{1}{V_\infty} D_{jx}^{Im} p_{n_p}^2 - D_{jx}^{Re} p_{n_p}) \end{bmatrix} \tag{70}$$

$$\tag{71}$$

$$\begin{aligned} F_f^{\text{aero}} = \ ...+ \left[I_{ff}, ..., I_{ff} \right] \cdot \left(s\mathbf{I} - \begin{bmatrix} -p_1 I_{ff} & & \\ & \ddots & \\ & & -p_{n_p} I_{ff} \end{bmatrix} \right)^{-1} \cdot \\ \begin{bmatrix} \bar{q} S_{fj} Q_{jj}^{(L_1)} (\frac{1}{V_\infty} D_{jf}^{Im} p_1^2 - D_{jf}^{Re} p_1) & \bar{q} S_{fj} Q_{jj}^{(L_1)} (\frac{1}{V_\infty} D_{jx}^{Im} p_1^2 - D_{jx}^{Re} p_1) \\ \vdots & \vdots \\ \bar{q} S_{fj} Q_{jj}^{(L_{n_p})} (\frac{1}{V_\infty} D_{jf}^{Im} p_{n_p}^2 - D_{jf}^{Re} p_{n_p}) & \bar{q} S_{fj} Q_{jj}^{(L_{n_p})} (\frac{1}{V_\infty} D_{jx}^{Im} p_{n_p}^2 - D_{jx}^{Re} p_{n_p}) \end{bmatrix} \cdot \begin{bmatrix} q_f \\ u_x \end{bmatrix} \end{aligned} \tag{72}$$

Acknowledgments

The author thanks Thiemo Kier for his valuable suggestions and stimulating conversations that greatly enhanced this work. The author, Jonas Eichelsdörfer, received a scholarship by Munich Aerospace e.V.

References

[1] Tewari, A., *Aeroservoelasticity*, SpringerLink, Springer, New York, NY [u.a.], 2015.

[2] Thompson, and Kass, "Active Flutter Suppression - An Emerging Technology," *Journal of Aircraft*, Vol. 9, No. 3, 1972, pp. 230–235. https://doi.org/10.2514/3.58962.

[3] Livne, E., "Aircraft Active Flutter Suppression: State of the Art and Technology Maturation Needs," *Journal of Aircraft*, Vol. 55, No. 1, 2018, pp. 410–452. https://doi.org/10.2514/1.c034442.

[4] Butz, H., Friedrichs, R., Jens and; Henke, and Hornung, M., "The Energy-Efficient Aircraft of the Future – A Long-Term Perspective," Tech. rep., The German Society for Aeronautics and Astronautics, 2025.

[5] Schmidt, D. K., "Stability Augmentation and Active Flutter Suppression of a Flexible Flying-Wing Drone," *Journal of Guidance, Control, and Dynamics*, Vol. 39, No. 3, 2016, pp. 409–422. https://doi.org/10.2514/1.g001484.

[6] Svoboda, F., and Hromcik, M., "Active flutter suppression by means of fixed-order H Infinity control: results for the Benchmark Active Control Technology (BACT) wing," *2019 18th European Control Conference (ECC)*, IEEE, 2019, pp. 119–124. https://doi.org/10.23919/ecc.2019.8795733.

[7] Theis, J., Pfifer, H., and Seiler, P. J., "Robust Control Design for Active Flutter Suppression," *AIAA Atmospheric Flight Mechanics Conference*, American Institute of Aeronautics and Astronautics, 2016. https://doi.org/10.2514/6.2016-1751.

[8] Pusch, M., Ossmann, D., and Luspay, T., "Structured Control Design for a Highly Flexible Flutter Demonstrator," *Aerospace*, Vol. 6, No. 3, 2019, p. 27. https://doi.org/10.3390/aerospace6030027.

[9] Schmidt, M. W. D., "Modeling and Model Simplification of Aeroelastic Vehicles," Tech. rep., 1992.

[10] Grauer, J. A., and Waite, J., "Design of a Collocation-Based Active Flutter Suppression Control Law for the IAWTM Wind Tunnel Model," *AIAA SCITECH 2024 Forum*, American Institute of Aeronautics and Astronautics, 2024. https://doi.org/10.2514/6.2024-2201.

[11] Ricci, S., Toffol, F., De Gaspari, A., Marchetti, L., Fonte, F., Riccobene, L., Mantegazza, P., Berg, J., Livne, E., and Morgansen, K., "Wind Tunnel System for Active Flutter Suppression Research: Overview and Insights," *AIAA Journal*, Vol. 60, No. 12, 2022, pp. 6692–6714. https://doi.org/10.2514/1.j061985.

[12] Stalla, F., Kier, T. M., Looye, G., and Pusch, M., "Aeroservoelastic Modeling and Robust Control for Gust Load Alleviation of an Experimental Wing," *AIAA SCITECH 2024 Forum*, American Institute of Aeronautics and Astronautics, 2024. https://doi.org/10.2514/6.2024-1442.

[13] Theodorsen, T., "General theory of aerodynamic instability and the mechanism of flutter," NACA Report 496, 1934. P.413–433.

[14] Peters, D., "Two-dimensional incompressible unsteady airfoil theory—An overview," *Journal of Fluids and Structures*, Vol. 24, No. 3, 2008, pp. 295–312. https://doi.org/10.1016/j.jfluidstructs.2007.09.001.

[15] Ohta, H., Fujimori, A., Nikiforuk, P. N., and Gupta, M. M., "Active flutter suppression for two-dimensional airfoils," *Journal of Guidance, Control, and Dynamics*, Vol. 12, No. 2, 1989, pp. 188–194. https://doi.org/10.2514/3.20390.

[16] Karpel, M., "Design for Active Flutter Suppression and Gust Alleviation Using State-Space Aeroelastic Modeling," *Journal of Aircraft*, Vol. 19, No. 3, 1982, pp. 221–227. https://doi.org/10.2514/3.57379.

[17] Nissim, E., "Flutter suppression using active controls based on the concept of aerodynamic energy," Tech. rep., NASA, 1971.

[18] Wright, J., and Cooper, J., *Introduction to aircraft aeroelasticity and loads*, second edition ed., Aerospace series, Wiley, Chichester, West Sussex, England, 2015. Includes bibliographical references and index.

[19] Albano, E., and Rodden, W., "A doublet-lattice method for calculating lift distributions on oscillating surfaces in subsonic flows." *AIAA Journal*, Vol. 7, No. 2, 1969, pp. 279–285. https://doi.org/10.2514/3.5086.

[20] Roger, K. L., Hodges, G. E., and Felt, L., "Active Flutter Suppression-A Flight Test Demonstration," *Journal of Aircraft*, Vol. 12, No. 6, 1975, pp. 551–556. https://doi.org/10.2514/3.59833.

[21] Roger, "Structural Aspects of Active Controls." *Agard Conference Proceedings*, 1977.

[22] Blair, M., "A Compilation of the Mathematics Leading to the Doublet Lattice Method," Tech. rep., Air Force Wright Laboratory, 1992.

[23] Kier, T., and Looye, G., "Unifying Manoeuvre and Gust Loads Analysis Models," *International Forum on Aeroelasticity and Structural Dynamics (IFASD)*, 2009.

[24] Bisplinghoff, R. L., *Aeroelasticity*, Dover science books, Dover, New York, 1996. Edited by Holt Ashley and Robert L. Halfman.

[25] Fung, Y. C., *An introduction to the theory of aeroelasticity*, Dover Publications, 2008.

[26] Hamdan, A. M. A., and Nayfeh, A. H., "Measures of modal controllability and observability for first- and second-order linear systems," *Journal of Guidance, Control, and Dynamics*, Vol. 12, No. 3, 1989, pp. 421–428. https://doi.org/10.2514/3.20424.

[27] Stein, G., "Respect the Unstable," *IEEE Control Systems*, Vol. 23, No. 4, 2003, pp. 12–25. https://doi.org/10.1109/mcs.2003.1213600.

[28] Horikawa, H., and Dowell, E. H., "An Elementary Explanation of the Flutter Mechanism with Active Feedback Controls," *Journal of Aircraft*, Vol. 16, No. 4, 1979, pp. 225–232. https://doi.org/10.2514/3.58509.

[29] Skogestad, S., and Postlethwaite, I., *Multivariable feedback control*, 2nd ed., Wiley, Chichester, 2010.

[30] Eichelsdörfer, J., "Modal Blending for Active Flutter Suppression," *submitted for AIAA Scitech 2026 Forum*, 2026.